Nanoscale

Accepted Manuscript

This article can be cited before page numbers have been issued, to do this please use: A. Nassereddine, L. Delannoy, C. Louis, G. Wang, D. Alloyeau, C. Ricolleau, A. Wilson and J. Nelayah, *Nanoscale*, 2026, DOI: 10.1039/D6NR00549G.

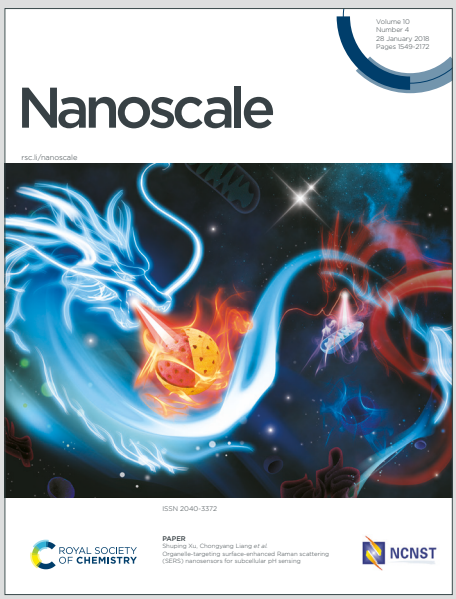

ROYAL SOCIETY OF CHEMISTRY

rsc.li/nanoscale

View Article Online
DOI: 10.1039/D6NR00549G

ARTICLE

Operando TEM study of a working TiO_2 supported Au and Au–Cu catalysts during butadiene hydrogenation

Received 00th January 20xx,
Accepted 00th January 20xx

DOI: 10.1039/x0xx00000x

Abdallah Nassereddine,*[a,b] Laurent Delannoy,†[c] Catherine Louis,[c] Guillaume Wang,[a] Damien Alloyeau,[a] Christian Ricolleau,[a] Axel Wilson [a] and Jaysen Nelayah*[a]

Understanding the structural stability and chemical dynamics of supported metal nanoparticles under working conditions is essential for the rational design of selective hydrogenation catalysts. In this work, we investigate monometallic Au/TiO_2 and bimetallic Au–Cu/TiO_2 catalysts during the selective hydrogenation of 1,3-butadiene using operando environmental scanning transmission electron microscopy (STEM) combined with mass spectrometry. Real-time imaging under atmospheric pressure and temperatures up to 400 °C reveals markedly different stability and sintering behaviors between the two catalysts, while the simultaneous mass spectrometry measurements confirm butadiene conversion and butene formation under reaction conditions. Monometallic Au nanoparticles remain highly stable on TiO_2, showing negligible sintering and limited morphological evolution up to 400 °C. In contrast, Au–Cu nanoparticles undergo pronounced temperature-dependent restructuring, including Ostwald ripening at 300 °C and a distinct growth mechanism at 400 °C, attributed to the reduction and reincorporation of mobile copper species into the alloy. Atomic-scale STEM analyses demonstrate that both Au and Au–Cu nanoparticles preserve an face-centered cubic structure during reaction, while copper enrichment within Au–Cu nanoparticles is evidenced by lattice contraction at elevated temperature. These observations highlight the critical role of copper mobility and alloying effects in governing nanoparticle dynamics, hydrogen activation, and catalytic performance under reaction conditions. This operando study provides direct insights into the structure–reactivity relationships of Au-based catalysts and underscores the necessity of characterizing bimetallic systems under realistic working environments.

Introduction

Gold-based catalysts have attracted significant interest due to their remarkable catalytic performance in selective hydrogenation reactions, particularly in the hydrogenation of unsaturated hydrocarbons.[1,2] Such reactions are crucial for industrial processes, especially for purifying hydrocarbon streams contaminated with unsaturated impurities, like alkynes and dienes.[3,4] Historically, catalysts based on nickel were among the first studied extensively in this context,[5] followed by palladium (Pd) catalysts,[6,7] which became preferred due to their excellent ability to adsorb and dissociate molecular hydrogen (H_2). On the other hand, monometallic gold (Au) catalysts demonstrate remarkable selectivity but typically exhibit lower catalytic activity compared to Pd-based systems.[8,9,10,11] This limited activity arises primarily from their inferior hydrogen dissociation capabilities, which restricts their reaction rates despite their high selectivity.

Alloying Au with other metals, notably Cu, has emerged as a compelling strategy to enhance the catalytic activity, due to the superior H_2 activation properties.[6] Au-Cu catalysts have demonstrated excellent miscibility and synergistic catalytic properties superior to their monometallic equivalents.[12,13,14,15] In 2013, Lee *et al.*[16] reported that bimetallic Au–Cu/SBA-15 catalysts with various Cu/Au ratios (4, 3, and 0.33) significantly outperformed their monometallic counterparts (6.7 wt% Au/SBA-15 and 3 wt% Cu/SBA-15) in the selective hydrogenation of acetylene, especially the Au_3Cu sample between 160 and 200°C. Diffuse Reflectance Infrared Fourier Transform spectroscopy (DRIFT) revealed that incorporating Au rendered Cu more electron-deficient, which enhanced hydrogen activation and, in turn, boosted catalytic activity. Furthermore, diluting the Cu^+ species, known for strongly adsorbing alkynes, helped minimize C-C coupling side reactions and improved ethylene selectivity. Delannoy *et al.*[17] conducted a 20-hour stability test of Au-Cu/TiO_2 catalysts at 75°C and observed a gradual increase in butadiene to butenes conversion during the initial hours, especially pronounced for the $AuCu_3$/TiO_2 bimetallic catalyst with the highest copper content. They proposed that this activation results from the progressive segregation of copper, identified as the most active element, to the surface of the bimetallic NPs. Building on these observations, recent environmental transmission electron microscopy (ETEM) studies on monometallic Au/TiO_2 catalyst have

[a] Université Paris Cité, CNRS, Laboratoire Matériaux et Phénomènes Quantiques, 75013 Paris, France
[b] Present adress : Institut Néel, UPR 2940 CNRS- Université Grenoble Alpes, Grenoble F-38000, France
[c] Sorbonne Université, CNRS, Laboratoire de Réactivité de Surface, LRS, F-75005 Paris, France
† Dr. Laurent Delannoy deceased May 12, 2024.
Supplementary Information available: [details of any supplementary information available should be included here]. See DOI: 10.1039/x0xx00000x

View Article Online
DOI: 10.1039/D6NR00549G

revealed notable morphological changes under pure hydrogen[18] and pure butadiene (C_4H_6)[19] gas. Coupled with *ab initio* molecular dynamics (AIMD)[18] and Density Functional Theory (DFT)[19] simulations, these *in situ* findings have illustrated the dynamic nature of Au surfaces in reducing atmospheres. Subsequent DFT and AIMD simulations exploring the electronic and structural stability of random Au-Cu solid solution under H_2 exposure (200-400°C) have demonstrated that,[20] Cu atoms segregate from subsurface to surface sites. This segregation results in the formation of linear H–Cu–H–Cu chains in bridging positions, alternating with H–Au–H–Au chains. In the Au–Cu core, a local chemical ordering is predicted where Au atoms become surrounded by Cu. This reorganization is characterized by a rearrangement of atomic positions that favors the formation of locally ordered Au–Cu domains, with Au atoms preferentially coordinated by Cu atoms. Such configurations are expected to reduce the dynamic flexibility of the nanoparticle structure, thereby promoting greater structural stability while maintaining the face-centered cubic (FCC) lattice under H_2.[20] These previous studies have provided **(i)** new insights into the size and alloying effects on the reactivity of Au and Au–Cu NPs toward hydrogen and 1,3-butadiene molecules, and **(ii)** initial atomic-level information on how the structural properties of TiO_2 supported Au and Au-Cu NPs evolve under pure hydrogen and butadiene conditions. A precise atom-level picture of structure and chemical ordering in the presence of butadiene hydrogenation reaction mixture remains missing, which is crucial for understanding the intrinsic catalytic properties of Au–Cu/TiO_2 catalysts during reaction.

To address these remaining scientific gaps, we employed an *operando* approach by coupling scanning transmission electron microscopy (STEM) imaging with mass spectrometry, allowing a direct correlation between the structural transformations of Au and Au-Cu NPs and their catalytic behaviour under realistic butadiene hydrogenation conditions. In particular, low-magnification high-angle annular dark field (HAADF) and bright field (BF) STEM imaging allowed the visualization of nanoparticle sintering mechanisms and assess structural stability, revealing correlations between nanoparticle structure, morphology, and catalytic activity across a range of temperatures. Moreover, atomic-scale STEM-HAADF and STEM-BF imaging made possible the identification of the nature and structural dynamics of the active phases of Au and Au–Cu catalysts during reaction, providing deeper insights into how structural and alloying effects influence the performance of bimetallic Au–Cu. These observations allowed to distinguish between Ostwald ripening (OR) and particle migration-coalescence phenomena, highlighting the pivotal role of Cu in atomic mobility and sintering processes. The *operando* ETEM experiments were carried out using a Protochips Atmosphere™ high-pressure gas cell (HPGC),[21,22,23] under butadiene hydrogenation gas environment at atmospheric pressure and temperatures ranging from 120 to 400°C. The catalytic activity was monitored in real time through semi-quantitative measurements of butadiene consumption and butene formation, using mass spectrometry of the reaction effluent.

Experimental

Catalysts preparation

Monometallic Au and bimetallic AuCu NPs were deposited onto a commercial TiO_2 support (100% anatase, surface area = 50 $m^2 \cdot g^{-1}$) using the deposition–precipitation with urea (DPU) method, as previously detailed in literature.[24,25,26] In a typical procedure, 2 g of TiO_2 were dispersed in 150 mL of distilled water at 80 °C. An appropriate amount of $HAuCl_4 \cdot 3H_2O$ or a mixture of $HAuCl_4 \cdot 3H_2O$ and $Cu(NO_3)_2 \cdot 3H_2O$ precursors was then added to reach the desired metal loading (e.g., 6 wt% Au and an Au:Cu atomic ratio of 1:1). An excess of urea ($CO(NH_2)_2$) was introduced ([urea]/[metal] = 100), and the mixture was stirred at 80 °C for 20 h in the dark to avoid any uncontrolled reduction of gold. The resulting solid was collected by centrifugation, washed three times with distilled water to remove chloride residues, and dried under vacuum at room temperature (in the dark). Finally, an activation step was performed at 300 °C for 2 h under H_2 flow (100 $mL \cdot min^{-1}$) to reduce the metal precursors into active metallic nanoparticles, resulting in the final Au/TiO_2 and AuCu/TiO_2 catalysts. The resulting Au and AuCu NPs exhibited sizes ranging from 1 to 5 nm, with an average diameter of approximately 3.5 nm, as determined by STEM-HAADF imaging. The catalysts were then purged with pure N_2 and transferred to air before loading into the Protochips Atmosphere™ high-pressure gas cell (HPGC) for *operando* TEM experiments. A schematic illustration of the synthesis steps is provided in the Supplementary Information (Figure S3) to further clarify the procedure.

Operando Transmission Electron Microscopy

All *operando* transmission electron microscopy experiments were carried out on a double aberration-corrected JEOL ARM 200F microscope equipped with a cold field emission gun operating at 200 kV.[27] A Protochips Atmosphere™ high-pressure gas cell (HPGC) was used for *operando* STEM observations under realistic reaction conditions (up to atmospheric pressure). The HPGC comprises two silicon microchips (E-chips) aligned face-to-face in a closed-cell configuration. The smaller E-chip (2 mm × 2 mm × 300 µm) features a 50 nm-thick amorphous SiN window, whereas the larger E-chip (6 mm × 4.5 mm × 300 µm) carries a SiC membrane patterned with six electron-transparent windows (30 nm-thick SiN) for imaging. The catalyst powder (previously ground and ultrasonically dispersed in water) was drop-cast onto the large E-chip; after assembly of the cell, the butadiene hydrogenation gas environment (20% H_2/0.36% C_4H_6/79.64% He) was introduced under dynamic flow conditions. This gas composition was selected to match the reaction conditions previously used for TiO_2-supported Au, Cu and AuCu catalysts in selective butadiene hydrogenation, for which high selectivity toward butenes was already established for this catalyst family.[17] The HPGC outlet was continuously monitored by mass spectrometry using a Pfeiffer Vacuum "PrismaPro QMG 250 F1" Residual Gas Analyzer (RGA) to track reactants and products in real time (see Figure S4 for a schematic illustration of the JEOL ARM-200F microscope coupled with the mass spectrometer). A detailed discussion regarding the

RGA implementation with the high-pressure cell, pre-analysis purge protocols, and the stabilization of gas compositions is provided in Supplementary Section S1. This section also includes typical RGA spectra and a comparison between ETEM-based measurements and standard laboratory-scale catalytic tests to highlight key procedural differences. The sample was heated via resistive heating of the SiC membrane, and a closed-loop temperature control system ensured accurate temperature regulation. Imaging was performed in STEM mode using both high-angle annular dark-field (HAADF) and bright-field (BF) detectors, with a 20.5 mrad convergence semi-angle, a probe current of ~27 pA, and short pixel dwell times (2–3 µs) to minimize beam-induced damage. High-resolution images (2048 × 2048 pixels) were acquired at selected magnifications, and the electron beam was blanked between frames to further limit electron dose.

Results and discussion

Temperature-Ramp Sintering Dynamics of Au/TiO_2 and AuCu/TiO_2 Catalysts in Butadiene Hydrogenation

For structural analysis, our initial investigation focused on assessing the stability of Au/TiO_2 and AuCu/TiO_2 catalysts by examining the mobility and morphological stability of Au and AuCu NPs on their TiO_2 support. This assessment was first conducted under inert environment (Ar), and subsequently under 10^5 Pa of the butadiene hydrogenation gas environment, using low-magnification in situ HAADF-STEM imaging across various temperature intervals.

For Au/TiO_2 catalyst, multiple NPs within three distinct regions, labelled as regions 1,2 and 3 (marked by red circles in Figures 1.a–d) were continuously monitored over a period of 3 hours. During the experiment, Au NPs exhibited remarkable stability on the TiO_2 support, showing no significant particle growth or mobility up to 400 °C. Comparisons between images captured under inert conditions at 120°C (Figure 1a) and those during temperature ramping between 200 and 400°C in the reactive gas mixture (Figure 1b–d) confirm the absence of diffusion or sintering phenomena even at elevated temperatures. Such pronounced stability indicates strong interaction between Au nanoparticles and the TiO_2 support in reducing atmospheres, effectively preventing particle migration and coalescence. Ex situ particle-size distributions measured before and after catalysis, as shown in the size histogram in the Supporting Information (Figure S2), show no significant change for Au/TiO_2 (3.8 ± 0.9 nm after synthesis vs 3.5 ± 0.9 nm after catalysis), in agreement with the operando TEM observations.

To investigate the alloying effects on AuCu/TiO_2 catalyst stability, the sintering behavior of AuCu NPs under butadiene hydrogenation gas environment was also studied by low-magnification in situ HAADF-STEM imaging (Figure 2). Unlike Au NPs, multiple cases of AuCu NPs sintering were observed at high temperature under the reaction mixture. To guide the eye, the 14 tracked AuCu NPs, distributed across four zones (A, B, C, and D) of the support, are marked with red circles and numbered from 1 to 14. Comparing observations under Ar flow at 120 °C (Figure 2.a) and under butadiene hydrogenation gas environment (Figure 2.b) shows that the AuCu NPs are stable on the TiO_2 support at 200 °C. However, after 46 minutes of heating at 300 °C, a decrease in NP density was observed in all studied zones (A, B, C and D), along with an increase in the size of some NPs (Figure 2.c). This size variation results from the disappearance of smaller particles and the growth of larger neighbouring particles. Specifically, in zones A, B, and C, small NPs (3, 4, 9, and 14) disappeared, while larger adjacent particles (1, 5, 6, 7, 8, 10, 11, 12, and 13) increased in size. Unlike the behavior observed at 300 °C, the generalized increase in size observed at 400 °C cannot be explained solely by mass transfer among the initially visible AuCu nanoparticles in the field of view. This suggests the contribution of additional Cu-containing species present on the TiO_2 support but not resolved in the low-magnification HAADF-STEM images. We therefore propose that highly dispersed CuO_x/Cu species, formed by partial re-oxidation of Cu during air transfer prior to the operando TEM experiment, are reduced again under the butadiene hydrogenation gas environment at high temperature and subsequently incorporated into the AuCu nanoparticles, leading to the observed increase in particle volume. This interpretation is consistent with our recent in situ synchrotron XAS study, which showed that Cu is reduced to the metallic state under H_2 treatment, indicating that the CuO_x species considered here are more likely generated during *ex situ* air handling than present in the freshly reduced catalyst.[28] In this case, an ex situ particle-size distribution measured after catalysis would not necessarily reflect the operando state, because the Cu-containing phase may be modified during air exposure after the reaction. Therefore, the growth of AuCu nanoparticles is discussed here primarily on the basis of direct operando tracking under the reaction gas mixture.

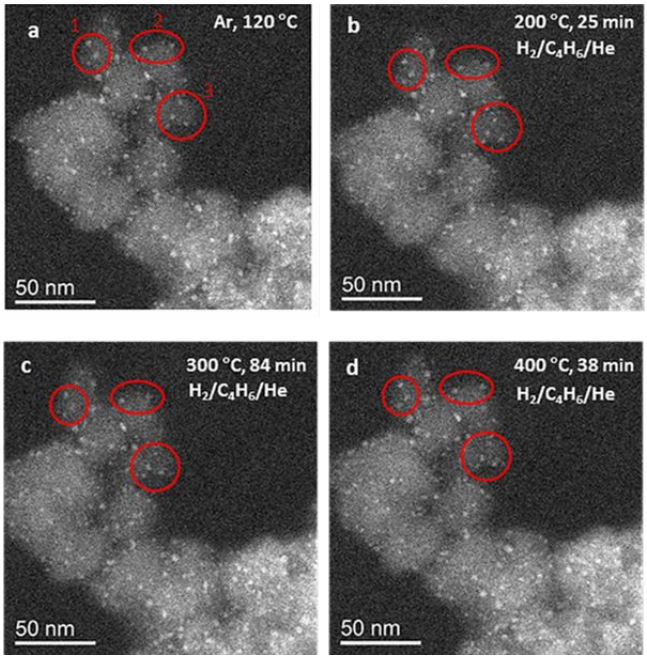

Figure 1. Stability test of dispersed Au NPs supported on TiO_2 during butadiene hydrogenation as a function of temperature. Sequences of low-magnification (500k) in situ HAADF-STEM images under a flow of: (a) 40 Pa of Ar at 120°C and

View Article Online
DOI: 10.1039/D6NR00549G

(b-d) 10^5 Pa (20% H_2/0.36% C_4H_6/79.64% He) mixture between 200 and 400°C as a function of time.

The sintering of AuCu NPs under the reaction mixture of butadiene hydrogenation (Figure 2) at 300 °C can be attributed to Ostwald ripening rather than particle migration and coalescence. Particle migration and coalescence require high NP mobility, which was not observed in our system. Instead, the disappearance of small NPs, coupled with concurrent growth of larger ones, is characteristic of Ostwald ripening, where atomic diffusion from smaller to larger NPs drives size evolution.[29,30,31]

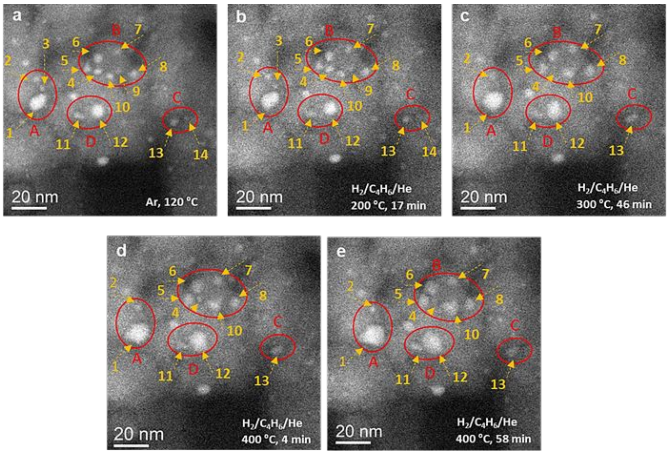

Figure 2. Stability test of dispersed AuCu NPs supported on TiO_2 during butadiene hydrogenation as a function of temperature. Low-magnification (500k) in situ HAADF-STEM images acquired under: (a) 40 Pa of Ar at 120°C and (b-e) 10^5 Pa of (20% H_2/0.36% C_4H_6/79.64% He) mixture at 200–400°C as a function of time.

The difference in sintering behavior between Au and AuCu NPs suggests that Cu plays a key role in facilitating atomic mobility at high temperatures.

For bimetallic nanoalloys, two types of Ostwald ripening can occur: Simple OR and Two-tier OR.[32,33] In the case of simple OR, both metal species exhibit similar atomic diffusion rates and evaporation energies, resulting in uniform ripening that preserves the overall atomic composition of the nanoparticles. In contrast, two-tier OR results from differences in atomic mobility, which combines two critical parameters: (1) the detachment energy of atoms from the nanoparticle surface and (2) the surface diffusion coefficient of the element. When one metal exhibits significantly higher atomic mobility (due to lower detachment energy and/or faster surface diffusion), preferential mass transfer occurs, affecting the NPs elemental distribution over time.

Several literature studies confirm that two-tier Oswald ripening in supported bimetallic NPs alters their atomic composition and leads to a size-dependent composition distribution. For instance, Alloyeau *et al.*[32] observed Co enrichment in large Co-Pt NPs deposited on carbon after vacuum annealing at 700°C, due to the higher evaporation rate of Co compared to Pt. Similarly, Di Vece *et al.*[34] showed Pd enrichment in Au-Pd NPs during hydrogen exposure at room temperature due to Pd lower cohesive energy and higher atomic mobility relative to Au. A similar phase-separation phenomenon has been reported by Prévot *et al.*[35] in Au-Pd NPs supported on amorphous carbon during annealing at 600 °C under vacuum. STEM-EDS measurements revealed the formation of two distinct populations: Au-rich NPs with a mean radius of 3.5 nm and large Pd-rich NPs with a mean radius of 25 nm. Despite the complete miscibility of the two metals, kinetic Monte Carlo simulations demonstrated that phase separation occurs due to the competition between surface energy and mixing enthalpy. The higher mobility of Pd atoms allows them to reach thermodynamic equilibrium during the coarsening process. Under a reducing environment (H_2), a comparable effect was observed by Piccolo *et al.*[36] who reported Pd enrichment in Ir-Pd NPs supported on SiO_2-Al_2O_3 at 350°C or 500°C. This further supports the hypothesis that bimetallic NP coarsening can lead to significant composition redistribution, influenced by external conditions such as temperature and gas environment.

In the present study, to estimate the relative detachment tendency of Au and Cu adatoms during Ostwald ripening mechanism, we followed the first-approximation approach proposed by Alloyeau *et al.*[32] in which evaporation the barrier is written as $\Delta E \approx Ea - Ec$, where Ea is the adsorption energy of an adatom on the support and Ec is the cohesive energy of the bulk metal, both expressed using the same sign convention. The cohesive energies Ec of bulk Cu and Au were therefore taken as Ec(Cu)= -3.49 eV/atom and Ec(Au)= -3.81 eV/atom, respectively.[37] Because the adsorption energies reported in the study of Yuan *et al.*[38] and Seriani *et al.*[39] use different conventions, they were first rewritten using a common sign convention before comparison. On the anatase TiO_2 (101) surface, the resulting adatom adsorption energies are Ea(Au) = −0.54 eV[38] and Ea(Cu) = −2.30 eV[39], leading to estimated detachment barriers of 3.27 eV for Au and 1.19 eV for Cu (see detailed calculation in the Section S3 in the Supporting Information). Conversely, on the anatase TiO_2 (001) surface, the corresponding values are Ea(Au) = −2.74 eV[38] and Ea(Cu) = −2.83 eV[39], giving estimated detachment barriers of 1.07 eV for Au and 0.66 eV for Cu. Additionally, while diffusion barriers for Au and Cu on TiO_2 remain uncertain in some contexts, previous DFT studies indicate that Au exhibits higher surface mobility on the anatase TiO_2 (101) surface, with a diffusion barrier of 0.24 eV, compared to 1.23 eV for Cu.[40] These theoretical considerations suggest that the exact Ostwald ripening mechanism (simple or two-tier) between 200 and 300°C strongly depends on the surface orientation of the anatase TiO_2 support.

Overall, the contrasting sintering behaviors of Au/TiO_2 and AuCu/TiO_2 highlight the impact of alloying on nanoparticle stability. While Au/TiO_2 remains structurally stable under hydrogenation conditions, AuCu/TiO_2 exhibits temperature-dependent sintering, with Cu atoms likely playing a significant role in facilitating atomic redistribution at high temperatures. Understanding these mechanisms is critical for designing sinter-resistant bimetallic catalysts for selective hydrogenation reactions.

Atomic visualization of active Au NPs structures under C_4H_6/H_2

Following the examination of nanoparticle sintering at lower magnification, we employed atomic-scale STEM imaging (STEM-HAADF and BF), complemented by Fast Fourier Transform (FFT) analyses, to capture structural dynamics at reaction temperatures ranging from 300 to 400°C, where significant catalytic activity was observed in Au (Figures 3.A and 4.A) and in Au-Cu (Figure 5.A)

Two representative Au NPs of 5.3 nm and 2.1 nm were analysed (Figures 3 and 4). In both cases, the mass spectrometry signals evolve during the initial temperature ramp between 120 and 200 °C, likely reflecting the progressive stabilization of the reactive gas environment and outlet detection in the high-pressure Protochips Atmosphere cell (Figure 3.A and 4.A). In addition, the narrow transfer capillaries used between the microscope holder outlet and the RGA inlet can introduce a delayed response during this initial transient stage. When the temperature reaches 300°C, a clear consumption of butadiene is observed, accompanied by a sharp increase in butene concentration. Upon further heating to 400°C, the $C_4H_6^+$ ion signal continues to decrease while the $C_4H_8^+$ signal stabilizes, suggesting a more active catalytic phase between 300°C and 400°C. The structural

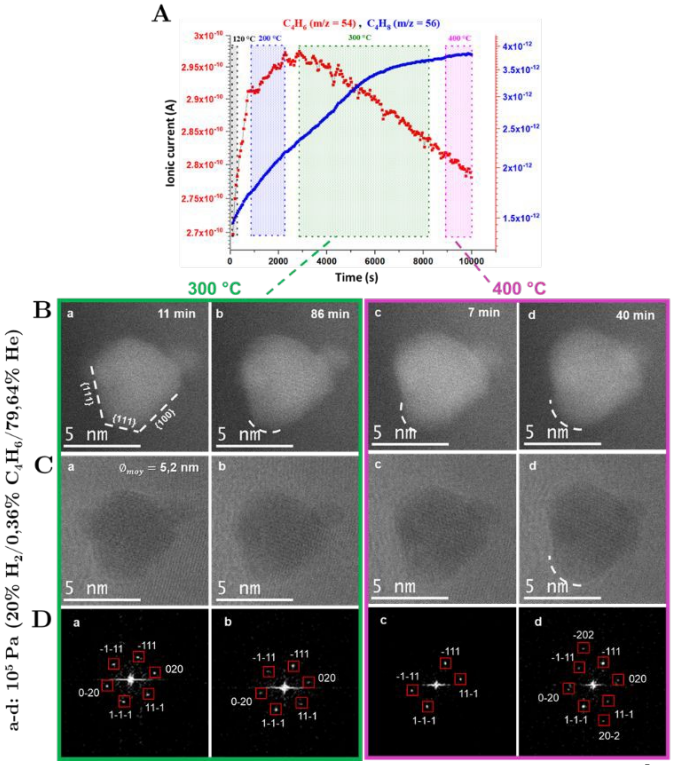

Figure 3. Structural evolution of a 5.3 nm Au nanoparticle under a gas flow of 10^5 Pa (20% H_2 / 0.36% C_4H_6 / 79.64% He. (A) Mass spectrometry monitoring of the evolution of butadiene (C_4H_6, m/z = 54) and butenes (C_4H_8, m/z = 56) concentrations during the temperature ramp from 120 to 400°C under continuous flow of the reactive gas mixture in the high-pressure Protochips Atmosphere cell. (B) Operando STEM-HAADF and (C) BF images acquired at 300°C (a,b) and 400°C (c,d) at different times. (D) FFT indexing of STEM-BF images shows that the nanoparticle has an FCC structure and is oriented along the [101] zone axis. The FCC structure remains stable between 300 and 400°C and retains its orientation during the butadiene hydrogenation reaction.

dynamics of the NPs were monitored in parallel during these two temperature stages (green zone for 300°C and purple zone for 400°C). After approximately 11 minutes at 300°C, STEM-HAADF and BF images (Figures 3.B,C) along with FFT analysis (Figure 3.D) indicated that the larger Au NP (5.3 nm) retained its FCC crystal structure. This NP was predominantly bounded by low-index facets (111) and (100) and aligned near the [101] zone axis. Although the FCC structure and crystallographic orientation remained stable during exposure to reaction conditions, minor morphological rounding at the edges between (111) and (100) facets occurred, particularly after extended exposure times at higher temperature (400°C), indicating subtle atomic-scale restructuring. In contrast, the smaller Au NP (2.1 nm, Figure 4) exhibited pronounced structural flexibility and morphological instability under the active phases range of the catalyst between 300 and 400°C. Initially stable in an FCC arrangement at 300 °C, the smaller Au nanoparticle exhibited progressive structural distortion during prolonged exposure at 400 °C. The filtered STEM-BF images and the corresponding Digital Micrograph intensity profiles (Figure 4.D,E) show a gradual loss of lattice-fringe periodicity, ultimately leading to the loss of its FCC structure and significant morphological rounding. This behavior is consistent with our previous in situ study under H_2, which showed that very small Au nanoparticles lose their FCC structure under hydrogen-rich conditions.[18]

Atomic visualization of active Au-Cu NPs structures under C_4H_6/H_2

To understand the influence of alloying effects on structural stability and morphology, we conducted analogous atomic-scale *operando* investigations on two representative AuCu nanoparticles (3 nm and 2.2 nm) under identical reaction conditions (Figures 5.B,C,D and 5.E,F,G respectively). As in the case of the Au/TiO_2 catalyst, the structural dynamics of the NPs in the AuCu/TiO_2 catalyst were monitored during the most active catalytic phase, between 300 and 400°C (Figure 5.A). Both AuCu NPs maintained their FCC structure throughout the experiment at 300°C and 400°C, as confirmed by STEM-HAADF, BF imaging, and FFT analysis (Figures 5.B,C,D.a and 5.E,F,G.a). A faint diffuse or fringe-like contrast can be seen close to the nanoparticle in some BF images (Figure 5C–c). In the present closed gas-cell geometry, this weak contrast may include projected contributions from the surrounding TiO_2 support and the amorphous SiN membrane. Although a minor carbonaceous contribution cannot be fully excluded, the BF images alone do not allow a clear identification of the origin of this contrast. Moreover, noticeable morphological changes associated with size increase were observed at elevated temperatures, particularly at 400°C. Interestingly, this growth was accompanied by an apparent decrease in the average lattice spacing estimated from the filtered STEM-BF images/FFT, from about 3.84 Å at 300 °C to about 3.79 Å at 400 °C. Given the nanoparticle size and the reduced contrast inherent to operando gas-cell imaging, these values should be regarded as approximate. Nevertheless, in view of Vegard's law,[41] this apparent contraction is qualitatively consistent with possible Cu enrichment within the alloyed nanoparticles at 400 °C, although it is not used here as stand-alone compositional proof.

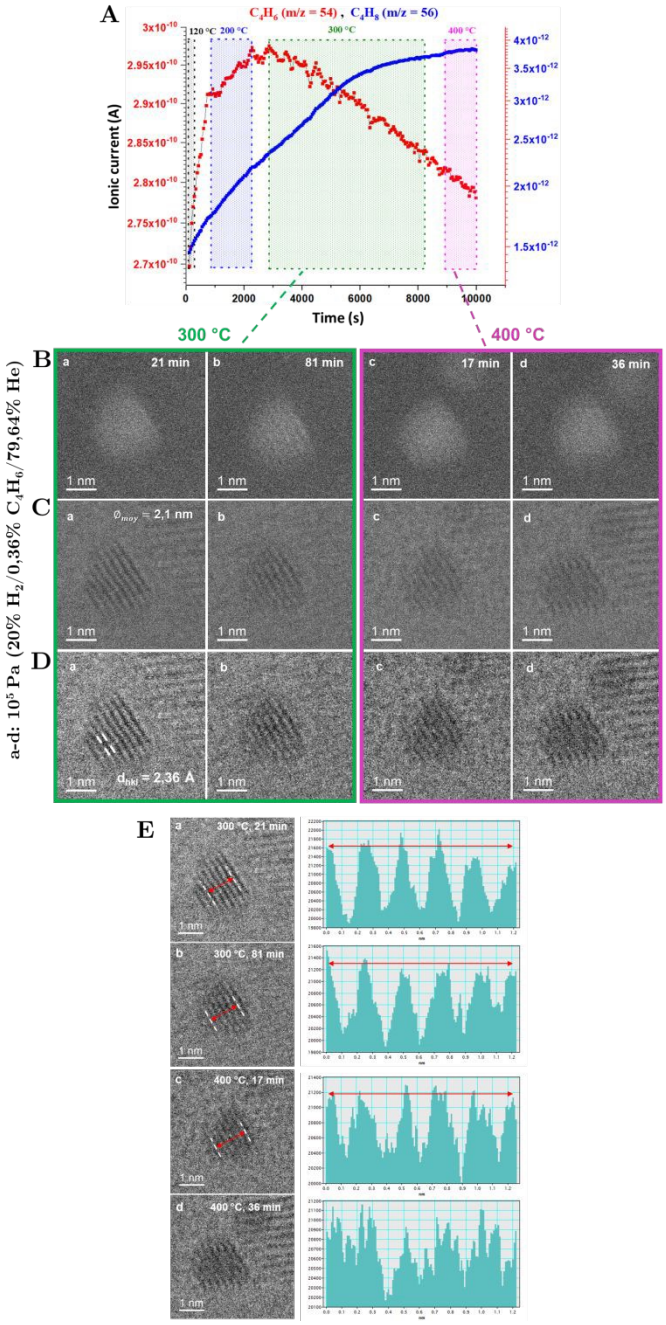

Figure 4. Structural evolution of a 2.1 nm Au nanoparticle under a gas flow of 10^5 Pa (20% H_2 / 0.36% C_4H_6 / 79.64% He). (A) Mass spectrometry monitoring of the evolution of butadiene (C_4H_6, m/z = 54) and butenes (C_4H_8, m/z = 56) concentrations during the temperature ramp from 120 to 400°C under continuous flow of the reactive gas mixture in the Protochips Atmosphere high-pressure cell. (B) operando STEM-HAADF and (C) BF images acquired at 300 °C (a,b) and 400 °C (c,d) at different times. (D) Filtered STEM-BF images. (E) Intensity profiles of the NPs lattice fringes extracted from the filtered STEM-BF images shown in (D). The intensity profiles reveal a loss of lattice fringe periodicity during the temperature increase, with the nanoparticle becoming fully distorted after 36 minutes at 400°C.

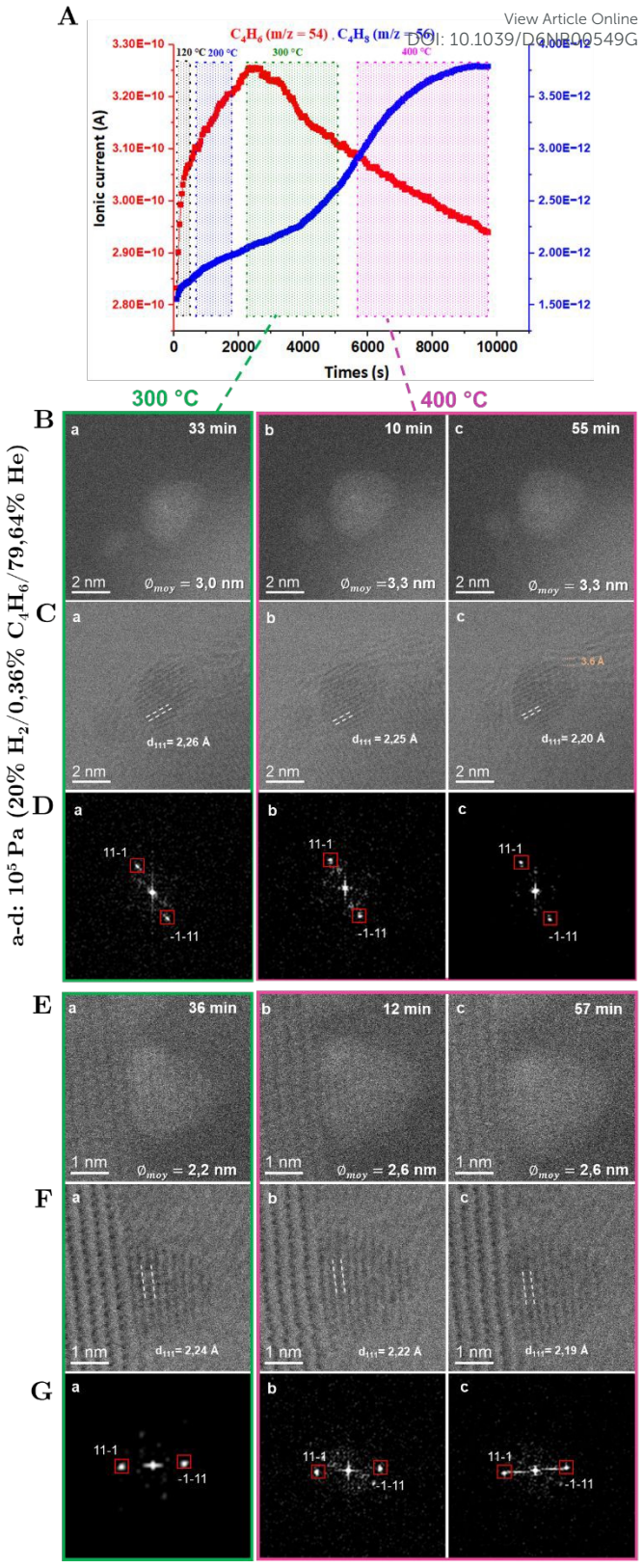

Figure 5. Structural evolution of two AuCu nanoparticles (2–5 nm) under a gas flow of 10^5 Pa (20% H_2 / 0.36% C_4H_6 / 79.64% He). (A) Mass spectrometry monitoring of the evolution of butadiene (C_4H_6, m/z = 54) and butenes (C_4H_8, m/z = 56) concentrations during the temperature ramp from 120 to 400 °C under continuous flow of the reactive gas mixture in the high-pressure Protochips Atmosphere cell. (B,C) operando STEM-HAADF and BF images of a 3 nm AuCu nanoparticle acquired at 300°C (a) and 400°C

View Article Online
DOI: 10.1039/D5NR00540G

(b,c) at different times. (E,F) In situ STEM-HAADF and BF images of a 2.2 nm AuCu nanoparticle acquired at 300°C (a) and 400°C (b,c) at different times. (D,G) FFT indexing of the STEM-BF images of both NPs shows that their FCC structure remains stable during butadiene hydrogenation as the temperature increases from 300 to 400°C.

Comparative discussion and catalytic implications

The catalytic performance in selective hydrogenation reactions strongly depends on hydrogen adsorption and dissociation, generally considered as rate-limiting steps.[9,42,43] Van Bokhoven *et al.*[10] demonstrated enhanced hydrogen adsorption capability at elevated temperatures, notably for smaller Au NPs (<4 nm). Moreover, combined ETEM and AIMD studies recently revealed structural transformations from FCC to icosahedral-like or other non-FCC structures for Au NPs smaller than 4 nm upon exposure to 10^5 Pa of hydrogen at 400 °C.[18] These smaller Au NPs showed strong reactivity with hydrogen, resulting in substantial morphological rounding and loss of crystalline structure between 200°C and 400°C. *Ab initio* molecular dynamics simulations further confirmed strong hydrogen interaction predominantly at low-coordination surface sites, driving these structural transitions. The *operando* TEM results align closely with these findings, reinforcing that smaller Au NPs undergo significant structural transformations at elevated temperatures, consistent with the enhanced catalytic response detected by mass spectrometry. This structural and morphological evolution highlights the critical role of nanoparticle size and hydrogen interaction strength in determining catalytic performance. In the present HPGC setup, these observations provide a qualitative link between the structural state of the Au NPs and the reactive regime detected by mass spectrometry.

Unlike monometallic Au/TiO_2 catalysts, where catalytic activity appears restricted predominantly to nanoparticles smaller than 4 nm, AuCu catalysts exhibited a more robust and less size-independent catalytic response. A central question for bimetallic AuCu catalysts under hydrogenation conditions is whether their activation is associated with a major Cu segregation process, potentially leading to surface-rich Cu domains or even to a core–shell-like reorganization. In this context, the present operando ETEM study provides direct structural information under the butadiene hydrogenation gas mixture. Our results show that the AuCu nanoparticles do not evolve toward complete phase separation. Instead, atomic-scale observations indicate that the nanoparticles remain alloyed, with a disordered solid-solution structure, under H2 reaction conditions. At no point do we observe the formation of a clear Au–Cu core–shell structure that would indicate strong Cu segregation at the nanoparticle surface. These observations suggest that the higher catalytic response of the bimetallic catalyst is associated with a dynamic alloyed state in which Cu mobility modifies the surface composition under reaction conditions, rather than with complete segregation into separated Au-rich and Cu-rich regions. Despite previous literature suggestions regarding copper surface segregation in AuCu systems, which is indeed predicted by our DFT calculations to occur at the surface under H_2 exposure,[20] it is crucial to note the contrast with the established thermodynamic equilibrium. Indeed, several literature studies combining atomistic calculations and thermodynamic approaches predict that, under vacuum conditions, the stable equilibrium structure of Au–Cu nanoparticles often involves Au enrichment at the surface, with a core that can show local chemical ordering.[44,45,46] This is also supported by recent experimental evidence by Breyton *et al.*[46] using energy dispersive X-ray analysis across (100) and (111) facets of Cu-Au NPs, demonstrating a complete segregation of Au in these facets for gold nominal compositions above 70% and 60%, respectively. This segregation behavior was observed in 10 nm sized nanoparticles grown by epitaxy on a salt surface and was found to be independent of nanoparticle size. This difference highlights that under reactive gas environments, the presence of H_2 gas modifies atomic interactions and mobilities, leading to leading to segregation behavior different from that observed in vacuum. This underscores the necessity of considering *operando* characterizations, as thermodynamic equilibria established in non-reactive environments may not directly translate to working catalytic systems.

Experimentally, despite the significant progress of ETEM, achieving a precise atomic picture and quantitative determination of the local surface composition of irregular AuCu nanoparticles under butadiene hydrogenation conditions remains beyond the current capabilities of *operando* TEM alone. Therefore, while the present observations clearly exclude complete phase separation or the formation of a well-defined Au–Cu core–shell structure, they do not rule out the possibility of partial Cu segregation at the nanoparticle surface. Such partial surface segregation is in fact consistent with our previous DFT study under pure H_2 conditions, which predicted Cu enrichment at the nanoparticle surface under hydrogen exposure.[20]

In conclusion, these atomic-scale observations provide direct insight into the structural state of Au and AuCu nanoparticles under butadiene hydrogenation conditions, highlighting the importance of nanoparticle size for Au and of Cu mobility/redistribution for AuCu. More specifically, the present *operando* study shows that the activation of the bimetallic catalyst is associated with a dynamic alloyed state under reaction conditions, rather than with complete Au/Cu phase separation. These findings provide important guidance for the optimization of selective hydrogenation catalysts through controlled alloying and operando control of surface composition.

Conclusions

In this study, operando environmental STEM combined with mass spectrometry has been employed to elucidate the structural and chemical evolution of Au/TiO_2 and Au–Cu/TiO_2 catalysts during the selective hydrogenation of 1,3-butadiene under realistic reaction conditions. Direct nanoscale and atomic-scale observations reveal a strong contrast in stability and dynamic behavior between monometallic and bimetallic systems. Monometallic Au nanoparticles exhibit remarkable structural stability on TiO_2, showing neither significant sintering nor particle migration up to 400 °C. While large Au nanoparticles retain their FCC structure with only minor surface

View Article Online
DOI: 10.1039/D6NR00549G

rounding, smaller Au nanoparticles display pronounced structural flexibility and partial loss of crystallinity at high temperature, correlating with increased catalytic activity. These results confirm the strong size dependence of hydrogen interaction and catalytic behavior in Au-based systems.

In contrast, Au–Cu nanoparticles undergo pronounced temperature-dependent restructuring under hydrogenation conditions. At 300 °C, sintering proceeds predominantly via Ostwald ripening, highlighting the enhanced atomic mobility induced by copper. At 400 °C, a different growth mechanism is observed, consistent with the reduction and reincorporation of copper species into the metallic phase. Despite these dynamic processes, Au–Cu nanoparticles maintain an FCC structure throughout the reaction, while lattice parameter contraction provides clear evidence of copper enrichment within the alloy at elevated temperature.

Overall, this work demonstrates that alloying Au with Cu profoundly modifies nanoparticle dynamics, surface composition, and catalytic behavior under operando conditions. The results emphasize that thermodynamic descriptions derived under vacuum or inert environments cannot fully capture the complexity of working catalysts exposed to reactive gas mixtures. By providing direct experimental insights into structure–reactivity relationships at the atomic scale, this study offers valuable guidelines for the rational design of more efficient and resilient bimetallic catalysts for selective hydrogenation reactions.

Author contributions

The manuscript was written through contributions of all authors. All authors have given approval to the final version of the manuscript.

Conflicts of interest

There are no conflicts to declare.

Data availability

The data that support the findings of this study are available from the corresponding author upon reasonable request. The data supporting this article have been included as part of the supplementary information (SI)

Acknowledgements

This work was supported by the French National Research Agency through the TOTEM project, Grant Number ANR-17-CE07-0031. A.N. was supported by a Ph.D. fellowship granted through the same project. The authors are grateful to Region Ile de France for convention SESAME E1845 for the support of the JEOL electron microscope installed at Université Paris Cité.

Notes and references

1 M. Juliusa, S. Robertsa and J. C. Q. Fletchera, *Gold Bull*, 2010, **43**, 298–306.
2 A. Corma and M. J. Sabater, in *Environmental Catalysis Over Gold-Based Materials*, eds. G. Avgouropoulos and T. Tabakova, The Royal Society of Chemistry, 2013, pp. 146–200.
3 S. A. Nikolaev, L. N. Zanaveskin, V. V. Smirnov, V. A. Averyanov and K. L. Zanaveskin, *Russ. Chem. Rev.*, 2009, **78**, 231–247.
4 P. R. Selvakannan, L. Hoang, V. V. Kumar, D. Dumbre, D. Jampaiah, J. Das and S. K. Bhargava, in *Catalysis for Clean Energy and Environmental Sustainability*, eds. K. K. Pant, S. K. Gupta and E. Ahmad, Springer International Publishing, Cham, 2021, pp. 205–228.
5 D. L. Trimm, I. O. Y. Liu and N. W. Cant, *Applied Catalysis A: General*, 2010, **374**, 58–64.
6 In *Advances in Catalysis*, Elsevier, 2019, vol. 64, pp. 1–88.
7 J. Goetz, M. A. Volpe, C. E. Gigola and R. Touroude, *Journal of Catalysis*, 2001, **199**, 338–345.
8 G. C. Bond, *Molecules*, 2012, **17**, 1716–1743.
9 E. Bus, J. T. Miller and J. A. Van Bokhoven, *J. Phys. Chem. B*, 2005, **109**, 14581–14587.
10 E. Bus and J. A. Van Bokhoven, *Phys. Chem. Chem. Phys.*, 2007, **9**, 2894–2902.
11 M. Manzoli, A. Chiorino, F. Vindigni and F. Boccuzzi, *Catalysis Today*, 2012, **181**, 62–67.
12 C. L. Bracey, P. R. Ellis and G. J. Hutchings, *Chem. Soc. Rev.*, 2009, **38**, 2231.
13 Y. Han, Y. Wang, T. Ma, W. Li, J. Zhang and M. Zhang, *Front. Chem. Sci. Eng.*, 2020, **14**, 689–748.
14 R. Ferrando, A. Fortunelli and R. L. Johnston, *Phys. Chem. Chem. Phys.*, 2008, **10**, 640–649.
15 M. Dhifallah, M. Iachella, A. Dhouib, F. Di Renzo, D. Loffreda and H. Guesmi, *J. Phys. Chem. C*, 2019, **123**, 4892–4902.
16 J. W. Lee, X. Liu and C. Mou, *J Chinese Chemical Soc*, 2013, **60**, 907–914.
17 L. Delannoy, G. Thrimurthulu, P. S. Reddy, C. Méthivier, J. Nelayah, B. M. Reddy, C. Ricolleau and C. Louis, *Phys. Chem. Chem. Phys.*, 2014, **16**, 26514–26527.
18 A. Nassereddine, Q. Wang, D. Loffreda, C. Ricolleau, D. Alloyeau, C. Louis, L. Delannoy, J. Nelayah and H. Guesmi, *Small*, 2021, **17**, 2104571.
19 A. Nassereddine, L. Delannoy, C. Ricolleau, C. Louis, D. Alloyeau, G. Wang, Q. Wang, H. Guesmi and J. Nelayah, *ChemCatChem*, 2023, **15**, e202300434.
20 Q. Wang, A. Nassereddine, D. Loffreda, C. Ricolleau, D. Alloyeau, C. Louis, L. Delannoy, J. Nelayah and H. Guesmi, *Faraday Discuss.*, 2023, **242**, 375–388.
21 J. F. Creemer, S. Helveg, P. J. Kooyman, A. M. Molenbroek, H. W. Zandbergen and P. M. Sarro, *J. Microelectromech. Syst.*, 2010, **19**, 254–264.
22 T. Alan, T. Yokosawa, J. Gaspar, G. Pandraud, O. Paul, F. Creemer, P. M. Sarro and H. W. Zandbergen, *Applied Physics Letters*, 2012, **100**, 081903.
23 O. Stamm, U. Latscha, P. Janecek and A. Campana, *Am J Obstet Gynecol*, 1976, **124**, 193–195.
24 R. Zanella, L. Delannoy and C. Louis, *Applied Catalysis A: General*, 2005, **291**, 62–72.
25 R. Zanella, *Journal of Catalysis*, 2004, **222**, 357–367.
26 R. Zanella, S. Giorgio, C. R. Henry and C. Louis, *J. Phys. Chem. B*, 2002, **106**, 7634–7642.

View Article Online
DOI: 10.1039/D6NR00549G

27 C. Ricolleau, J. Nelayah, T. Oikawa, Y. Kohno, N. Braidy, G. Wang, F. Hue, L. Florea, V. Pierron Bohnes and D. Alloyeau, *Microscopy (Tokyo)*, 2013, **62**, 283–293.
28 A. Nassereddine, L. Delannoy, X. Carrier, C. Louis, C. La Fontaine, A. Beauvois, J. Nelayah and A. Wilson, *ChemCatChem*, 2025, **17**, e202500379.
29 P. Wynblatt and N. A. Gjostein, *Acta Metallurgica*, 1976, **24**, 1165–1174.
30 A. K. Datye, Q. Xu, K. C. Kharas and J. M. McCarty, *Catalysis Today*, 2006, **111**, 59–67.
31 T. W. Hansen, A. T. DeLaRiva, S. R. Challa and A. K. Datye, *Acc. Chem. Res.*, 2013, **46**, 1720–1730.
32 D. Alloyeau, G. Prévot, Y. Le Bouar, T. Oikawa, C. Langlois, A. Loiseau and C. Ricolleau, *Phys. Rev. Lett.*, 2010, **105**, 255901.
33 J. Nelayah, N. T. Nguyen, D. Alloyeau, G. Y. Wang and C. Ricolleau, *Nanoscale*, 2014, **6**, 10423–10430.
34 M. Di Vece, S. Bals, J. Verbeeck, P. Lievens and G. Van Tendeloo, *Phys. Rev. B*, 2009, **80**, 125420.
35 G. Prévot, N. T. Nguyen, D. Alloyeau, C. Ricolleau and J. Nelayah, *ACS Nano*, 2016, **10**, 4127–4133.
36 L. Piccolo, S. Nassreddine, M. Aouine, C. Ulhaq and C. Geantet, *Journal of Catalysis*, 2012, **292**, 173–180.
37 C. Kittel, *Introduction to solid state physics*, Wiley, Hoboken, NJ, 8. ed., [repr.]., 20.
38 W. Yuan, D. Zhang, Y. Ou, K. Fang, B. Zhu, H. Yang, T. W. Hansen, J. B. Wagner, Z. Zhang, Y. Gao and Y. Wang, *Angewandte Chemie*, 2018, **130**, 17069–17073.
39 N. Seriani, C. Pinilla and Y. Crespo, *J. Phys. Chem. C*, 2015, **119**, 6696–6702.
40 A. Alghannam, C. L. Muhich and C. B. Musgrave, *Phys. Chem. Chem. Phys.*, 2017, **19**, 4541–4552.
41 L. Vegard, *Z. Physik*, 1921, **5**, 17–26.
42 R. Zanella, *Journal of Catalysis*, 2004, **223**, 328–339.
43 A. Hugon, L. Delannoy and C. Louis, *Gold Bull*, 2009, **42**, 310–320.
44 G. Guisbiers, S. Mejia-Rosales, S. Khanal, F. Ruiz-Zepeda, R. L. Whetten and M. José-Yacaman, *Nano Lett.*, 2014, **14**, 6718–6726.
45 J. Li, G. Wang and G. Zhou, *Surface Science*, 2016, **649**, 39–45.
46 G. Breyton, H. Amara, J. Nelayah, J. Creuze, H. Guesmi, D. Alloyeau, G. Wang and C. Ricolleau, *Phys. Rev. Lett.*, 2023, **130**, 236201.

View Article Online
DOI: 10.1039/D6NR00549G

Data availability

The data that support the findings of this study are available from the corresponding author upon reasonable request. The data supporting this article have been included as part of the supplementary information (SI)